








# Novel Reluctance-Type Magnetic-Geared Motor Integrated With High-Speed Bearingless Motor

Akira Kumashiro , Graduate Student Member, IEEE, Lingyu Chen , Member, IEEE, Yusuke Fujii , Member, IEEE, Akira Chiba , Fellow, IEEE, Wolfgang Gruber , Senior Member, IEEE, Wolfgang Amrhein , and Gerald Jungmayr 

**Abstract**—In this paper, a magnetic-geared motor with an integrated bearingless high-speed rotor is proposed. Active two-axis suspension forces are provided to the suspended high-speed rotor by three-phase suspension windings. The principles of magnetic suspension and torque generation are presented. In addition, the suspension characteristics are evaluated in 3-D finite element analysis. A test machine was built, and both magnetic suspension and rotation were verified. As a result, the principle of a magnetic-geared motor with a magnetically suspended bearingless high-speed rotor has been confirmed for the first time.

**Index Terms**—Bearingless motor, finite element method, magnetic gear, magnetic suspension, magnetic-geared motor.

## I. INTRODUCTION

THE combination of an electric motor and a mechanical gearbox is widely used. However, mechanical gearboxes transmit torque based on gear engagement. Thus, there are drawbacks, such as friction loss, tooth wear, and requirements of lubrication and periodic maintenance. In addition, the gear may be destroyed when overload is applied.

To solve these problems, magnetic-geared motors have been proposed by Chau et al. [1]. The magnetic-geared motor achieved almost identical torque density as that of a mechanical-geared motor [2], but without the friction losses at the gear teeth [3], [4], [5]. Subsequently, the magnetic-geared motors have a

potential to achieve high torque density as that of mechanical-geared motors, as shown in [5].

Meanwhile, the magnetic-geared motors of previous studies have mainly focused on the low-speed operation and high-torque density, such as 1500 r/min and 130 r/min on high-speed and low-speed rotors, respectively [4], and 575 r/min and 230 r/min on high-speed and low-speed rotors, respectively [6]. Meanwhile, some magnetic-geared motors have high-speed rotation. For example, the high-speed rotor reaches 14 000 r/min for automotive traction at an output of 100 kW [5]. In addition, it can reach up to 22 644 r/min at an output of 329.4 W for industrial motors [7]. In [7], it is shown that the mechanical bearing loss is as high as 20% of the total losses at high-speed rotation. Thus, the mechanical bearing loss of the high-speed rotor imposes a significant problem at high-rotational speed. In [8], a magnetically suspended magnetic gear has been proposed, although there was no active torque-generating function. Additionally, in terms of durability, the limited lifetime of mechanical bearings in the high-speed rotor is a problem.

To improve durability and decrease mechanical bearing loss, bearingless motors that eliminate mechanical bearings have been proposed for high-torque operation. In [9], a compact 26-pole and 24-slot bearingless motor for 1500 r/min rated speed has been reported. In [10], an eight-pole twelve-slot bearingless motor has been described. In [11], flux-switching bearingless motor for 1000 r/min. In [12], a multi-consequent-pole bearingless motor has been analyzed. In [13], a 20-pole 24-slot consequent-pole bearingless motor with parallel motor winding has been implemented for mixing applications. In [14], large scale bearingless motor is reported for 2000 r/min with the stator outer diameter and the stack length of 500 mm and 20 mm, respectively. However, the bearingless motors have limited applications since the rotor is suspended magnetically without mechanical contact. Thus, it is sensitive to changes in the rotor dynamics. Hence, bearingless motors are mainly implemented to applications with lightweight and short-shafted impellers or fan blades.

In this paper, a novel magnetic-geared motor integrated with a high-speed bearingless motor is proposed to eliminate the need for mechanical bearings in the high-speed rotor. In this topology, the structure of the magnetic-geared motor can be simplified. Furthermore, the durability and the efficiency problem of the mechanical high-speed rotor bearing is solved. In addition, this structure can transmit torque without mechanical contacts.

Manuscript received 19 June 2023; revised 24 October 2023; accepted 19 December 2023. Date of publication 23 January 2024; date of current version 21 May 2024. Paper 2023-EMC-0785.R1, presented at the 2022 International Power Electronics Conference, Himeji, Japan, May 15–19, and approved for publication in the IEEE TRANSACTIONS ON INDUSTRY APPLICATIONS by the Electric Machines Committee of the IEEE Industry Applications Society [DOI: 10.23919/IPEC-Himeji2022-ECCE53331.2022.9807141]. This work was supported in part by the LCM – K2 Center for Symbiotic Mechatronics within the framework of the Austrian COMET-K2 Program, in part by JST SPRING, under Grant JPMJSP2106, and in part by research grant from the Japan Power Academy. (Corresponding author: Akira Kumashiro.)

Akira Kumashiro, Lingyu Chen, Yusuke Fujii, and Akira Chiba are with the Department of the Electrical and Electronic Engineering, Tokyo Institute of Technology, Tokyo 152-8550, Japan (e-mail: kumashiro.a@belm.ee.titech.ac.jp; chen.l@belm.ee.titech.ac.jp; fujii@ee.e.titech.ac.jp; achiba@ieec.org).

Wolfgang Gruber and Wolfgang Amrhein are with the Institute of Electrical Drives and Power Electronics, Johannes Kepler University, 4040 Linz, Austria (e-mail: wolfgang.gruber@jku.at; wolfgang.amrhein@jku.at).

Gerald Jungmayr is with the Linz Center of Mechatronics, 4040 Linz, Austria (e-mail: gerald.jungmayr@lcm.at).

Color versions of one or more figures in this article are available at <https://doi.org/10.1109/TIA.2024.3357049>.

Digital Object Identifier 10.1109/TIA.2024.3357049

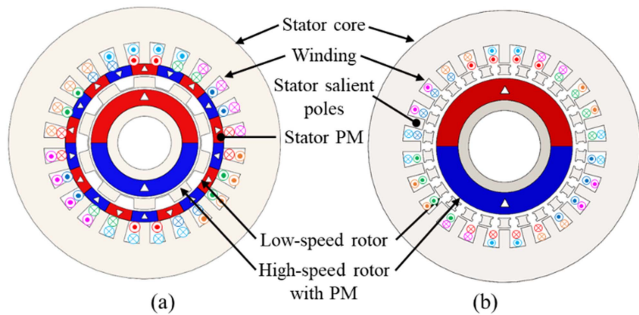


Fig. 1. Topology of a magnetic-geared motor of two different principles. (a) PM-type. (b) Reluctance type.

Moreover, the proposed motor has the possibility to enhance the torque density with the integrated magnetic gear compared to traditional bearingless motors. The concepts have been reported by the authors previously [15], [16], [17], [18]. In the proposed machine, only the radial positions of the magnetically suspended high-speed rotor is actively controlled with a compact structure. Thus, the proposed machine has a flat disc-type structure for passive magnetic suspension of the axial and the tilting directions. The stator has a three-phase suspension winding to regulate radial positions. The proposed machine has a two-pole magnetically suspended high-speed rotor to increase the gear ratio. Furthermore, the low-pole number of the rotor reduces the frequency of the inverter output, and the iron loss.

This transaction paper is based on the conference paper presented at the International Power Electronics Conference (IPEC-Himeji 2022 - ECCE Asia) in Himeji, 2022 [17]. In [17], a novel reluctance-type magnetic-geared motor integrated with a high-speed bearingless motor was introduced. As a result of the three-dimensional finite element method (3D-FEM) analysis, a suitable structure was found to generate stable radial suspension force. In this transaction paper, the new Section V has been added based on the comments provided at the presentation. A test machine was constructed, and stable magnetic suspension and rotation have been successfully achieved. Thus, the principle of the proposed reluctance-type magnetic-geared motor integrated with a high-speed bearingless motor has been confirmed by experiments.

## II. INTEGRATION WITH HIGH-SPEED BEARINGLESS MOTOR AND MAGNETIC-GEARED MOTOR

Recently, many magnetic-geared motor papers have been proposed. These papers propose various magnetic-geared motor topologies. In view of the number of parts with permanent magnets (PMs), the magnetic-geared motor topologies can be divided into two: PM type, with PMs in two parts [1], [3], [4], [5], and reluctance type, with PMs in one part [6]. Fig. 1 shows the cross-sectional view of each topology. In the reluctance type, the torque density is significantly reduced compared to the PM type [19], [20], [21]. However, the magnet resistance is reduced due to the decrease of PMs in the flux path of the winding flux. In magnetic-geared motors, the motor current density is relatively small compared to the other PM motors [3]. Nevertheless, the

TABLE I  
TORQUE DENSITY COMPARISON OF THE TWO-AXIS ACTIVELY CONTROLLED BEARINGLESS MOTORS

Ref.	[24]	This paper	[11]	[9]	[14]
Volume (cm <sup>3</sup> )	31	<b>154</b>	556	3927	3927
Outer diameter (mm)	63	<b>140</b>	266	500	500
Axial Length(mm)	10	<b>10</b>	10	20	20
Torque (Nm)	0.022	<b>0.499</b>	1.00	13.1	15.0
Torque density(kNm/m <sup>3</sup> )	0.71	<b>3.2</b>	1.8	3.3	3.8
Rated speed (r/min)	-	<b>1000</b>	1000	1500	2000

requirement for suspension current is significant compared to the motor current. In consequence, the slot space of the proposed motor is reduced to a reasonable size by selecting the reluctance type. Additionally, the characteristics of the magnetic-geared motor integrated with a bearingless motor have not been experimentally validated. The PMs with high pole-number have a risk of generating disturbances due to mechanical and magnetic misalignment. By contrast, the reluctance-type magnetic-geared motors have a simple structure. Therefore, the reluctance-type magnetic-geared motor is suitable for initial characteristics validation. Compared to the Vernier motors, the flux per current of the proposed motor is less due to the existence of two air gaps. Meanwhile, the power factor is increased since the motor winding pole-number is identical as that of the rotor PM pole-number [22].

In magnetic-geared motors, the torque density is a crucial factor. The torque density of an early magnetic-geared motor in [3] was above 60 kNm/m<sup>3</sup>. In contrast, the bearingless motors tend to have rather low-torque density because torque generation and magnetic suspension generation are integrated. In addition, bearingless motors with two or less actively controlled axes have low torque densities [23]. For example, in two-axis actively controlled bearingless motors, the rotor must have a flat disc-shape to increase the passive magnetic suspension characteristics; these are tilting and axial movements. The passive magnetic suspension is realized by significant fringing fluxes. As a result, the air gap flux density is decreased. Thus, torque density is also decreased. Table I shows the comparison of the two-axis actively controlled bearingless motors in the literature and this article. According to Table I, the torque densities are less than 4 kNm/m<sup>3</sup>. In the bearingless motors with large diameter, the torque density is relatively high. Meanwhile, it is challenging to achieve high torque density in a motor having a smaller diameter such as the proposed motor. Therefore, the utilization of the magnetic-geared motor with bearingless motor is effective.

## III. OPERATION PRINCIPLE

### A. Proposed Structure

Fig. 2 shows a cross-sectional view of the proposed magnetic-geared motor integrated with a high-speed bearingless motor. It consists of three parts: a bearingless high-speed rotor, a low-speed rotor, and a stator core with windings. The high-speed rotor consists of a permanent magnet (PM) featuring  $p_h$  pole

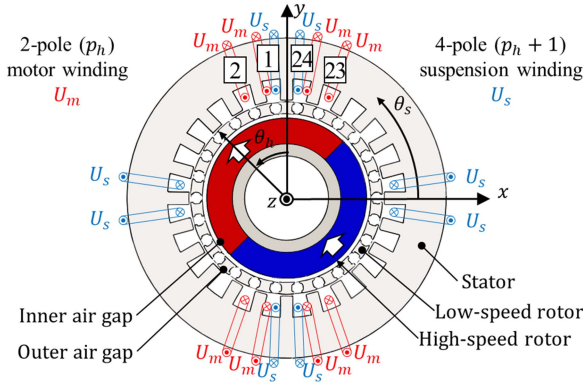


Fig. 2. Cross-sectional view of the proposed motor.

pairs. Radial forces are known to be generated by the interaction of  $p$  and  $p \pm 1$  pole-pairs magnetic flux. In this motor, the magnetic-suspended rotor is the high-speed rotor with  $p_h$  pole-pairs. Thus, the three-phase suspension winding creates  $p_h \pm 1$  pole-pairs in addition to the three-phase torque winding that creates  $p_h$  pole-pairs. These windings are both installed in the  $n_s$  slots to generate torque and suspension force simultaneously. The low-speed rotor is composed of  $n_l$  salient poles of laminated silicon steel blocks. The low-speed rotor is supported by mechanical bearings. The low-speed rotor generates torque through its interaction with the high-speed rotor and the stator.

In this paper, the pole-pair combination of the high-speed rotor PM, the low-speed rotor salient poles, the stator teeth, and the suspension winding are chosen as  $p_h = 1$ ,  $n_l = 26$ ,  $n_s = 24$ , and 2 respectively. The reason for choosing the pole combinations is explained in Section III-B and C.

### B. Operational Principle of Reluctance Magnetic-Geared Motor

In a magnetic-geared motor without PMs in the stator [6], [15], [16], [17], [18], [25], the low-speed rotor and the stator teeth cause the modulation of the magnetic flux. Let us define the stator angular coordinate  $\theta_s$ . The mean and amplitude of the stator permeance are given by  $P_{s0}$  and  $P_{s1}$ , respectively. Then, the permeance distribution  $P_s(\theta_s)$  is expressed as

$$P_s(\theta_s) = P_{s0} + P_{s1} \cos(n_s \theta_s). \quad (1)$$

Let us assume the mean and amplitude of the low-speed rotor permeance distribution are given by  $P_{l0}$  and  $P_{l1}$ , respectively. The angular velocity of the low-speed rotor is assumed as  $\omega_l$ , and the deviation angle between the  $x$ -axis and the center of the low-speed rotor iron piece is  $\delta_l$  at  $t = 0$ . Consequently, the permeance  $P_l(\theta_s, t)$  of the low-speed rotor is expressed as

$$P_l(\theta_s, t) = P_{l0} + P_{l1} \cos[n_l(\theta_s - \omega_l t - \delta_l)]. \quad (2)$$

Let us assume that the magnetomotive force amplitude of the PMs of the high-speed rotor is  $F_{h1}$ . Additionally, the angular velocity of the high-speed rotor is  $\omega_h$ , and the deviation angle between the  $x$ -axis and the magnetization direction of the high-speed rotor PM is  $\delta_h$  at  $t = 0$ . Consequently, the magnetomotive

force  $F_h(\theta_s, t)$  of the high-speed rotor is expressed as

$$F_h(\theta_s, t) = F_{h1} \cos[p_h(\theta_s - \omega_h t - \delta_h)]. \quad (3)$$

From (1) and (3), the flux-density distribution  $B_{sh}(\theta_s, t)$  of the outer air gap, located between the low-speed rotor and the stator, is obtained as

$$\begin{aligned} B_{sh}(\theta_s, t) &= P_s(\theta_s) F_h(\theta_s, t) \\ &= \{P_{s0} + P_{s1} \cos(n_s \theta_s)\} F_{h1} \cos[p_h(\theta_s - \omega_h t - \delta_h)] \\ &= F_{h1} P_{s0} \cos[p_h(\theta_s - \omega_h t - \delta_h)] \\ &\quad + \frac{F_{h1} P_{s1}}{2} \cos[(n_s + p_h)\theta_s - p_h \omega_h t - p_h \delta_h] \\ &\quad + \frac{F_{h1} P_{s1}}{2} \cos[(n_s - p_h)\theta_s + p_h \omega_h t + p_h \delta_h]. \end{aligned} \quad (4)$$

From (2) and (3), the flux-density distribution  $B_{lh}(\theta_s, t)$  in the same air gap can be also obtained as

$$\begin{aligned} B_{lh}(\theta_s, t) &= P_l(\theta_s, t) F_h(\theta_s, t) \\ &= \{P_{l0} + P_{l1} \cos[n_l(\theta_s - \omega_l t - \delta_l)]\} F_{h1} \cos[p_h(\theta_s - \omega_h t - \delta_h)] \\ &= F_{h1} P_{l0} \cos[p_h(\theta_s - \omega_h t - \delta_h)] \\ &\quad + \frac{F_{h1} P_{l1}}{2} \cos[(n_l + p_h)\theta_s - (p_h \omega_h + n_l \omega_l)t - (p_h \delta_h + n_l \delta_l)] \\ &\quad + \frac{F_{h1} P_{l1}}{2} \cos[(n_l - p_h)\theta_s + (p_h \omega_h - n_l \omega_l)t + (p_h \delta_h - n_l \delta_l)]. \end{aligned} \quad (5)$$

Note that both (4) and (5) are flux-density distributions at the same air gap. Hence, the coefficients of  $\theta_s$  at the second or third term in (4) must be identical to the second or third term in (5). Thus, the following relation must be satisfied

$$|n_s \pm p_h| = |n_l \pm p_h|. \quad (6)$$

Equation (6) contains eight states. However, half of these states can be neglected to satisfy  $n_s \neq n_l$  and  $n_s > 0$ ,  $n_l > 0$ . Thus, (6) can be expressed as,

$$\begin{cases} n_s + p_h = n_l - p_h \\ n_s - p_h = n_l + p_h \\ -n_s + p_h = n_l - p_h \\ -n_s - p_h = n_l + p_h \end{cases}. \quad (7)$$

Equation (7) can be simplified as,

$$|n_l \pm n_s| = 2p_h. \quad (8)$$

Moreover, to transmit torque between high-speed and low-speed rotors continuously, the coefficients of  $t$  at the second or third term in (4) must be identical to the second or third term in (5). Thus, the following relation must be satisfied

$$2p_h \omega_h = \pm n_l \omega_l. \quad (9)$$

From (9), the gear ratio  $G_r$  is given as

$$G_r = \frac{\omega_h}{\omega_l} = \pm \frac{n_l}{2p_h}. \quad (10)$$



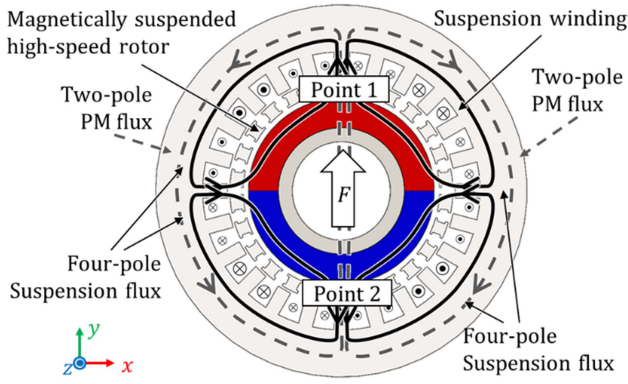


Fig. 3. Principle of radial-force generation.

According to (10), the gear ratio is proportional to  $n_l$  and inversely proportional to  $p_h$ . Thus, the small  $p_h$  and large  $n_l$  model is suitable to achieve a high gear ratio. Therefore, the condition of (8) in the proposed machine is chosen as

$$n_l - n_s = 2p_h. \quad (11)$$

To increase the gear ratio, the number of the high-speed rotor PM is chosen as one. In addition, to avoid the generation of the unnecessary harmonics by the motor and suspension winding, the stator slot number is chosen as  $6n$ . Additionally, the maximum stator teeth number is limited since the stator teeth width is also limited. Thus, the pole combination is chosen as  $p_h = 1, n_l = 26, n_s = 24$ .

In addition, this leads to a gear ratio  $G_r$  of 13 in this prototype. The output torque of the low-speed rotor is 13 times of the high-speed rotor torque.

Let us assume that the torque of the high-speed rotor and low-speed rotor are  $T_h$  and  $T_l$ , respectively. The maximum transmission torque of the high-speed rotor is  $T_{hmax}$ . Thus, each rotor torque with  $\omega_h = G_r \omega_l$  condition is expressed as,

$$\begin{cases} T_h = T_{hmax} \sin(-n_l \delta_l + 2p_h \delta_h) \\ T_l = T_{hmax} G_r \sin(n_l \delta_l - 2p_h \delta_h) \end{cases}. \quad (12)$$

The torques depend on  $n_l \delta_l - 2p_h \delta_h$ . This parameter behaves as the load angle in a synchronous motor. Hence, let  $n_l \delta_l - 2p_h \delta_h$  be defined as the magnetic gear load angle  $\delta_g$ . Thus, (12) can be expressed as,

$$\begin{cases} T_h = -T_{hmax} \sin(2\delta_g) \\ T_l = T_{hmax} G_r \sin(2\delta_g) \end{cases}. \quad (13)$$

### C. Principle of Magnetic Suspension

In the proposed motor, the high-speed rotor is magnetically suspended by the principle of the two-axis actively position regulated surface-mounted permanent magnet bearingless motor [10], [14], [26], [27], [28], [29], [30]. In this kind of magnetic suspension, only the  $x$ - and  $y$ -axis positions of the rotor are regulated by the  $p_h \pm 1$  pole-pair suspension winding. Meanwhile, the other degrees of freedom, which are the  $z$ -axis, the tilting  $\theta_x$ , and  $\theta_y$ , are passively stabilized using the reluctance forces generated by the PMs.

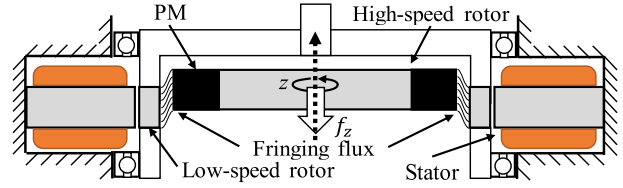


Fig. 4. Principle of passive magnetic suspension force generation in the axial direction.

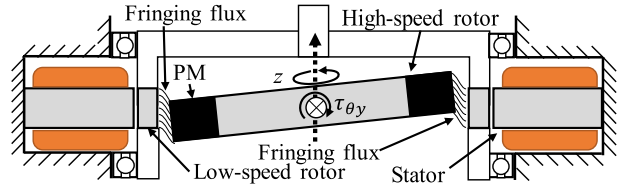


Fig. 5. Principle of passive magnetic suspension force generation in the tilting direction.

Fig. 3 shows the principle of suspension-force generation in the proposed motor. Let us suppose that the rotor is centered with zero suspension current and that the flux-density distribution of the air gap is symmetrical. Thus, the amplitude of the air-gap flux density is identical at points 1 and 2. In this case, the attraction forces cancel each other, and the overall radial force on the rotor is zero. When a three-phase suspension current is applied in the suspension winding as shown in Fig. 3, the radial force is generated in positive  $y$ -axis direction, because the air-gap flux density is increased and decreased at points 1 and 2, respectively. For suspension current in the opposite direction as shown in Fig. 3, a negative  $y$ -axis force is generated. The  $x$ -axis force is generated by providing current in the four-pole winding perpendicular to the one shown in Fig. 3. In this case, the radial force is basically proportional to the suspension current. With the feedback of the rotor radial position, the radial force is controlled for stable non-contact magnetic suspension.

As previously mentioned, the interaction between  $p$  and  $p \pm 1$  pole-pair magnetic flux generates radial forces. From (4) and (5), the proposed motor topology generates magnetic flux harmonics, specifically  $n_s \pm p_h$  and  $n_l \pm p_h$ . Thus, these harmonics must avoid the  $p_h \pm 1$  order to prevent interaction. Furthermore, to prevent radial force generation with no suspension current in the centered position, a symmetry factor  $x_s$  is important for selecting the pole combination previously presented by a part of the authors [31]

$$x_s = \gcd(2p_h, n_s) = \gcd(2p_h, n_l) = 2. \quad (14)$$

If  $x_s > 1$ , the magnetic gear does not produce radial force in the centered position. Hence, the proposed motor can achieve magnetic suspension without suspension current when the rotor is centered theoretically. In this paper, the pole combination is chosen based on (14).

To achieve stable magnetic suspension, the error angle of the radial active force must be as small as possible. Let us assume that the reference suspension force is  $\mathbf{F}^* = [F_x^* \ F_y^*]^T$  and the actual suspension force generated by applying the suspension current is  $\mathbf{F} = [F_x \ F_y]^T$ . The error angle  $\theta_{err}$  can be



TABLE II  
SPECIFICATIONS OF THE ANALYZED MODEL

Parameter	Unit	Value
Stator outer diameter	mm	130/140
Stator inner diameter	mm	86
Slot depth	mm	9.3
High-speed rotor outer diameter $D$	mm	70
Low-speed rotor radial thickness	mm	5
Stack length $L$	mm	10
Inner air-gap length	mm	2
Touchdown length of the high-speed rotor	mm	0.5
Outer air-gap length	mm	1
Turn number of motor winding	-	12
Turn number of suspension winding	-	21
Winding diameter	mm	0.4
Stator core material	-	20HX1300
Low-speed rotor material	-	20HX1300
High-speed rotor PM material	-	N48
High-speed rotor core material	-	S45C

TABLE III  
PARAMETERS OF THE PROTOTYPE MACHINE

Parameter	Symbol	Unit	Value
Rotor mass	$m$	kg	0.23
Maximum torque of low-speed rotor	$T_l$	Nm	0.499
Maximum tilting stiffness	$k_{\theta max}$	N/rad	17.0
Minimum tilting stiffness	$k_{\theta min}$	N/rad	5.0
Motor power factor (at $N_l = 2,000$ r/min)	$\cos\theta_m$	-	96.2%
Coil resistance in $ma$ - and $mb$ - axis	$R_{ma}$	$\Omega$	0.443
Coil inductance in $ma$ - and $mb$ - axis	$L_{ma}$	mH	0.980
Coil resistance in $sa$ - and $sb$ - axis	$R_{sa}$	$\Omega$	0.622
Coil inductance in $sa$ - and $sb$ - axis	$L_{sa}$	mH	1.059

expressed as

$$\theta_{err} = \tan^{-1} \left( \frac{F_y}{F_x} \right) - \tan^{-1} \left( \frac{F_y^*}{F_x^*} \right). \quad (15)$$

Figs. 4 and 5 show the principle of passive magnetic suspension force generation in axial and tilting directions, respectively. When the rotor is displaced in the axial direction, a restoring force  $f_z$  is generated due to the fringing magnetic flux on the edge of the rotor PM. Similarly, when the rotor is displaced in tilting direction, a restoring torque  $\tau_{\theta y}$  is generated. To improve the stiffness in the tilting direction, the rotor axial length should be thin, and the rotor diameter should be large. Therefore, in the two-axis actively controlled bearingless motor, the stack length is typically disc-type to stabilize the rotor passively.

#### IV. 3D-FEM ANALYSIS RESULT

##### A. Analysis Settings

To investigate the influence of stator yoke thickness on the magnetic suspension performance, a 3D-FEM transient magnetic field analysis (using JMAG-Designer 20.2, JSOL corp.) was conducted under the specification shown in Table III. Fig. 6 shows the flux and the mesh condition. In this model, the stack length is thin to enhance the passive suspension characteristics. As a result, the edge effect and fringing flux effect are not negligible [18] as shown in Fig. 6(a). Thus, a 3D-FEM is necessary

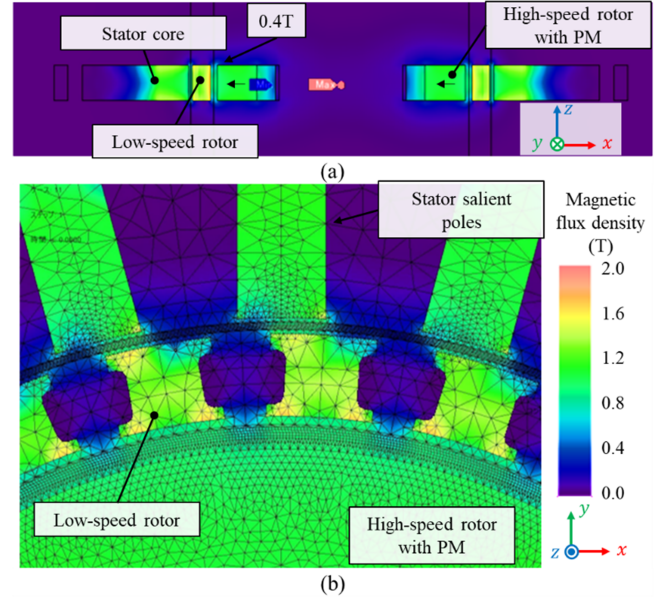


Fig. 6. Flux-density distribution of the 140 mm outer diameter model. (a) Flux leakage distribution in  $x$ - $z$  cross-section. (b) Mesh view around the air gaps.

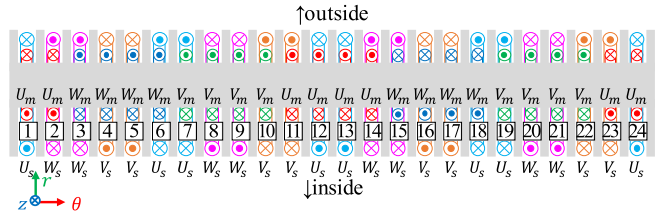


Fig. 7. Winding arrangement of the analyzed model.

for this model. The analyses are conducted by dividing one revolution into 90 segments, because the torque and radial force ripple are small [17]. Most of the analyses except for the unbalanced magnetic pull force analysis are conducted at the centered position. When switched off, the rotor is generally touched-down to the radial position determined by the touchdown clearance. In order to start the magnetic suspension, the FEM analysis was carried out to check if the magnetic suspension can be possible at the limited starting current. The FEM mesh is automatically generated considering the rotor radial displacement.

The windings of the model employed the toroidal winding to reduce the end winding. In two-axis actively controlled bearingless motor, the end winding length must be short since a flat disc-type rotor is required for passive stabilization [32], [33], [34]. The conductors located at the inside of the stator yoke are effective in generating magnetomotive force. Meanwhile, the conductors located at the outside of the stator yoke are not effective in generating magnetomotive force.

The numbers of strand in the suspension and motor windings are both five. Fig. 7 shows the winding arrangement of the proposed motor. The number indicates the slot numbers corresponding to those Fig. 2. Every slot has a motor conductor and a suspension conductor. The number of the conductors in the slots is evenly distributed.

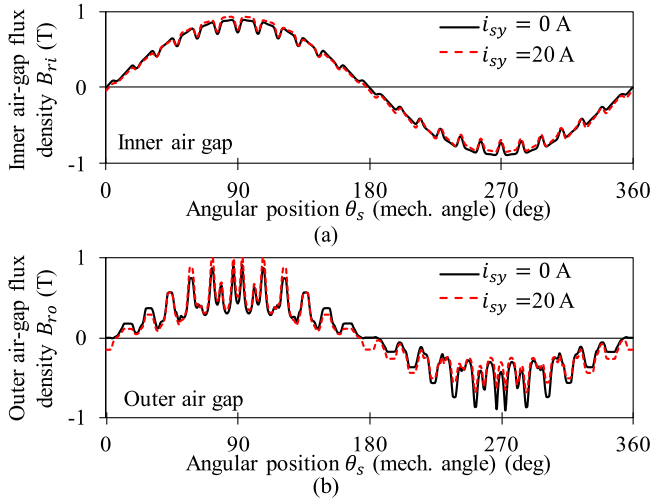


Fig. 8. Air-gap flux-density distributions in the radial direction. (a) Inner air gap: Between high-speed rotor and low-speed rotor. (b) Outer air gap: Between low-speed rotor and stator.

In this machine, the two-axis position is actively regulated. Thus, the diameter of the suspended high-speed rotor  $D$  is set as 70 mm and the stack length  $L$  is set as 10 mm to stabilize the rotor passively. Hence, the aspect ratio  $D/L = 7$ .

The 0-degree rotational angle of the high-speed rotor  $\theta_h$  in this paper is defined as the position where the  $y$ -axis aligns with the magnetization direction of the PM.

### B. Air-Gap Flux-Density Distribution

The flux-density distribution in the two air gaps was analyzed. As described in Section III-B, the spatial harmonics of the flux density verify flux modulation of the magnetic gear. Also, as described in Section III-C, the flux density must be asymmetrical when suspension current is applied.

Fig. 8 shows the radial flux-density distributions in the two air gaps. The black solid line and the red dashed line show the flux densities at the suspension currents  $i_{sy}$  of 0 A and 20 A, respectively. Fig. 8(a) shows the inner air-gap flux density  $B_{ri}$  between the high-speed and low-speed rotors. When  $i_{sy}$  is 20 A, the flux density  $B_{ri}$  is increased around  $\theta_s = 90^\circ$  although it is reduced around  $\theta_s = 270^\circ$ . This unbalanced air-gap flux density generates radial suspension force in the  $\theta_s = 90^\circ$  direction. Fig. 8(b) shows the outer air-gap flux density  $B_{ro}$  between the low-speed rotor and stator. There is an increase and decrease in the flux density at  $\theta_s = 90^\circ$  and  $\theta_s = 270^\circ$  as in case of Fig. 8(a). This result shows that the radial force is generated in the low-speed rotor when the suspension force is generated in the high-speed rotor. The radial force in the low-speed rotor is supported by the ball bearings.

Fig. 9 shows the magnitudes of the spatial harmonic components of the flux density  $B_{ro}$  in the outer air gap. The 2<sup>nd</sup> component, corresponding to  $p_h + 1$  in Section III-C, is created by the suspension current. Also, harmonic fluxes are generated such as 23<sup>rd</sup>, 25<sup>th</sup>, and 27<sup>th</sup>. These components are generated by the modulation due to the stator teeth and the low-speed rotor as shown in (4) and (5).

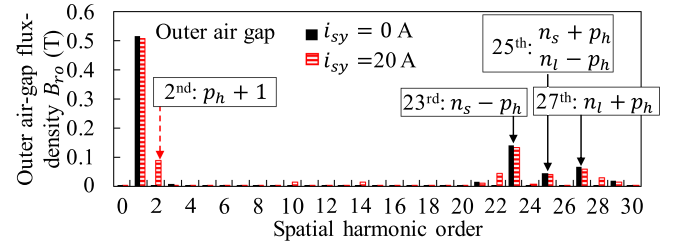


Fig. 9. Magnitudes of flux density in spatial harmonic components between the low-speed rotor and stator.

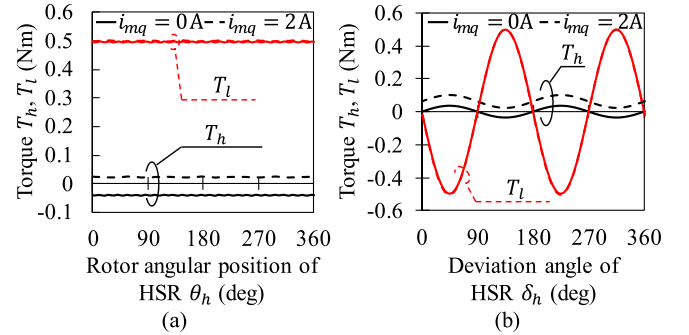


Fig. 10. Torque waveform in different conditions with and without  $q$ -axis current  $i_{mq}$ . (a) Synchronous rotation with respect to the rotational angular position of the high-speed rotor (HSR)  $\theta_h$ . (b) Low-speed rotor is fixed and the deviation angle of the high-speed rotor (HSR)  $\delta_h$  is changed.

Fig. 10 shows the torque waveform with and without  $q$ -axis current  $i_{mq}$ . According to Fig. 10, the  $q$ -axis current  $i_{mq}$  affects only the high-speed rotor torque. Fig. 10(a) shows the torque under  $\delta_g = \pi/2$  and synchronous  $\omega_h = G_r \omega_l$  conditions, which produces the maximum torque of the low-speed rotor continuously. From this figure, the torque ripple is small, less than 1% for all waveforms, and (13) condition is verified. Additionally, when  $i_{mq}$  is applied, counter-torque is compensated and this model acts as a geared motor. Fig. 10(b) shows the torque under  $\delta_l = 0$  and  $\delta_h$  is changed from 0 to  $2\pi$ , which means that the low-speed rotor is locked and only the high-speed rotor is rotated. This waveform validates (12). Note that the low-speed rotor salient poles number  $n_l$  is an even number, thus that waveform is the second-order sinusoidal wave.

### C. Stator Back Yoke and Suspension Force

To compare the suspension characteristics, analyses with different yoke thicknesses are conducted. In this model, the pole number of the magnetic suspension flux is significantly lower than the number of the low-speed rotor pole pieces. Thus, the suspension characteristics are not dependent on the  $\delta_l$  and  $\delta_h$ . Hence, these analyses are conducted in  $\delta_g = 0$  condition. Figs. 11 and 12 show the flux-density distribution when the suspension force is generated towards positive  $y$ -axis. To reduce the error angle  $\theta_{err}$ , the stator must avoid flux density saturation to increase suspension flux. Thus, the flux density of the stator yoke must be small when no suspension current is applied. In the 130 mm outer diameter model, the maximum value of the flux density in the stator yoke is 1.67 T. In the 140 mm outer diameter model, it is decreased to 1.50 T since the thickness of

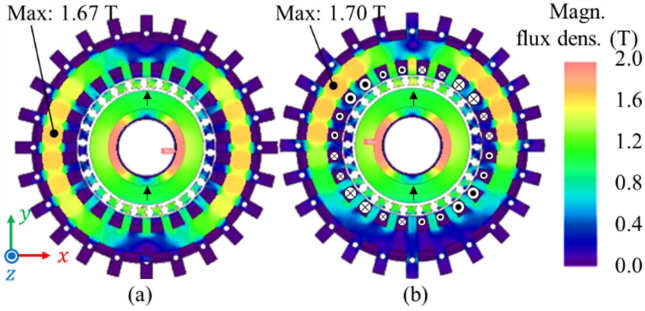


Fig. 11. Flux-density distribution of the 130 mm outer diameter model at suspension current  $i_{sy}$  of (a) 0 and (b) 20 A.

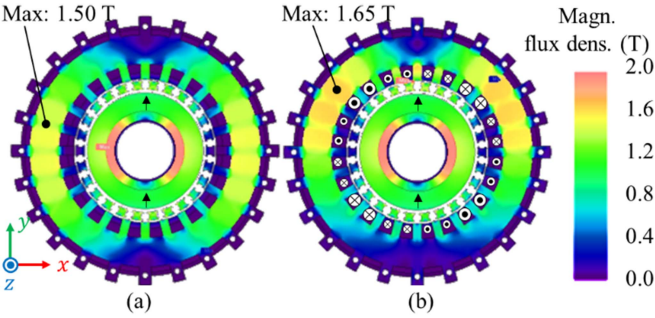


Fig. 12. Flux-density distribution of the 140 mm outer diameter model at suspension current  $i_{sy}$  of (a) 0 and (b) 20 A.

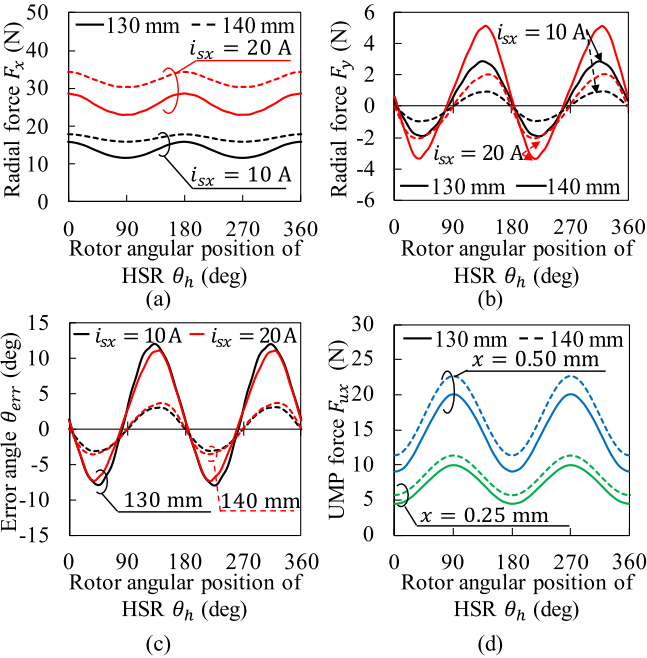


Fig. 13. Suspension characteristics with respect to the rotational angular position of the high-speed rotor (HSR)  $\theta_h$ . (a) Suspension force  $F_x$ . (b) Suspension force  $F_y$ . (c) Error angle  $\theta_{err}$ . (d) Unbalanced magnetic pull (UMP) force  $F_{ux}$ .

the stator yoke is enlarged and higher suspension fluxes can be applied.

Fig. 13 shows the suspension characteristics of the proposed motor for each model. In Fig. 13(a) and (b), the generated suspension forces are shown at the suspension current  $i_{sx} = 10$  A

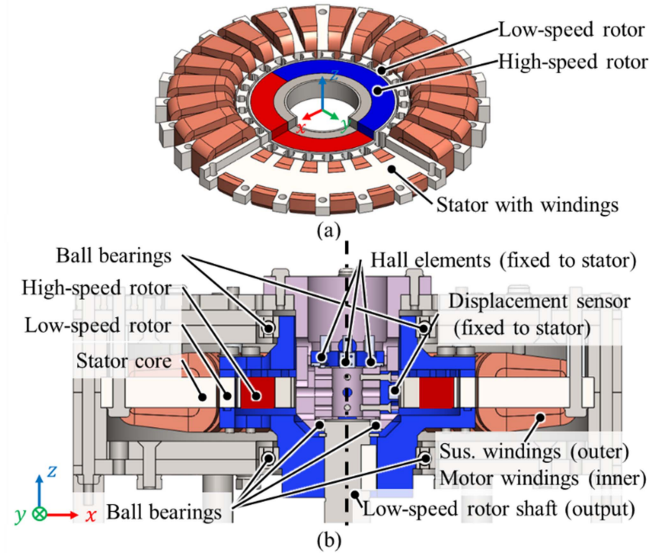


Fig. 14. Prototype model. (a) Isometric projection drawing. (b) Cross-sectional view.

and 20 A. Fig. 13(a) and (b) show the radial force  $F_x$  and  $F_y$  in  $x$ - and  $y$ -axis directions, respectively. In Fig. 13(a), the averages  $\bar{F}_x$  of the radial force in the  $x$ -axis direction at  $i_{sy} = 20$  A are 25.9 N and 32.2 N for the 130 mm and 140 mm outer diameter models, respectively. Fig. 13(c) shows the error angle  $\theta_{err}$ , as defined in (15). In Fig. 13(c), the error angle  $\theta_{err}$  does not depend on the suspension current, whereas the error angle of the 140 mm model is smaller than that of the 130 mm outer diameter model. Thus, in terms of suspension performance, a thick stator back yoke is favorable. Fig. 13(d) shows the unbalanced magnetic pull force  $F_{ux}$ , that is the  $x$ -axis radial force and the rotor radial displacement  $x$  in the high-speed rotor. In Fig. 13(d), the averages of the unbalanced pull force  $\bar{F}_{ux}$  at the radial displacement 0.50 mm are 14.4 N and 17.3 N for the 130 mm and 140 mm outer diameter models, respectively.

From Fig. 13(a) and (d), the most critical conditions for the magnetic suspension are around  $\theta_h = 90^\circ$  and  $270^\circ$ , where the lowest suspension force and the highest unbalanced pull force are generated. Thus, the maximum start-up current is 17.7 A and 15.0 A for the 130 mm and 140 mm outer diameter models, respectively.

## V. EXPERIMENT

### A. Experimental Setup

A prototype motor was fabricated to evaluate the analysis results. The prototype machine consists of a stator with an outer diameter of 140 mm. Table III shows parameters of the prototype machine. The all values are calculated from analysis result and CAD model. Fig. 14 shows the CAD model. Fig. 15 shows the manufactured experimental setup. The motor and suspension windings are separated and are each supplied from two different three-phase inverters. The high-speed rotor PMs are made of N48 material, and the outside is covered with 1 mm thick carbon fiber reinforced plastic. The stator and the low-speed rotor core



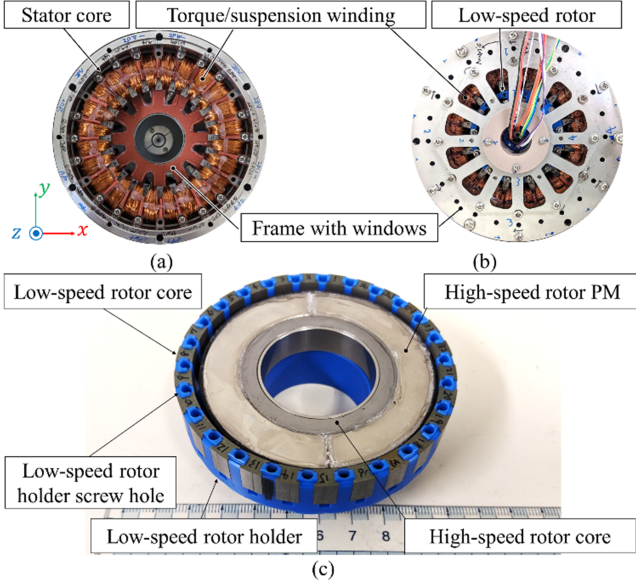


Fig. 15. Prototype of the proposed machine. (a) Stator with winding and frame. (b) Assembled machine. (c) High-speed rotor and low-speed rotor.

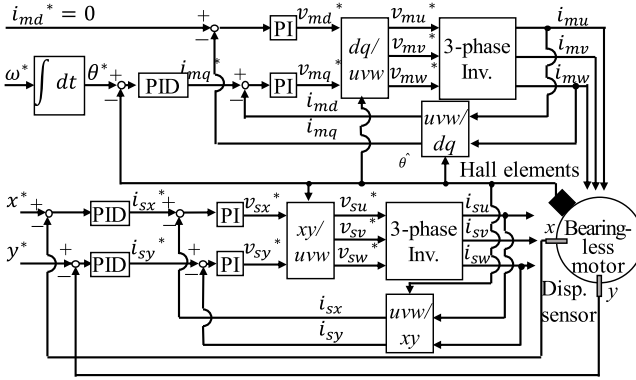


Fig. 16. Control system for rotor radial position and current.

are made of laminated silicon steel 20HTH1200. Meanwhile, the high-speed rotor core is made of S45C material because the iron loss is negligible. The frame and low-speed-rotor holder, which are not part of the magnetic circuit, are made of non-magnetic SUS304 stainless steel and MC901 nylon plastic, respectively.

Fig. 16 shows the radial position and current control system. The superscript (\*) and the subscripts (m), and (s) denote the reference, motor, and suspension, respectively. The motor and suspension current references are generated from the feedback signals. In the magnetic suspension, eddy current displacement sensors (PU-03A, AEC) are used to measure the rotor displacement. The errors of the radial rotor positions are calculated from the measured radial positions  $x$  and  $y$  and the position references  $x^*$  and  $y^*$ . The  $x$ - and  $y$ -axis current references  $i_{sx}^*$  and  $i_{sy}^*$  are generated from the errors of the radial positions by PID controller with a first-order low-pass filter in the derivative path. The voltage commands  $v_{sx}^*$  and  $v_{sy}^*$  are generated by nested PI controller. These voltage commands are transformed to the three-phase voltage references  $v_{su}^*$ ,  $v_{sv}^*$ , and  $v_{sw}^*$ , and then impressed into the windings by the inverters to regulate

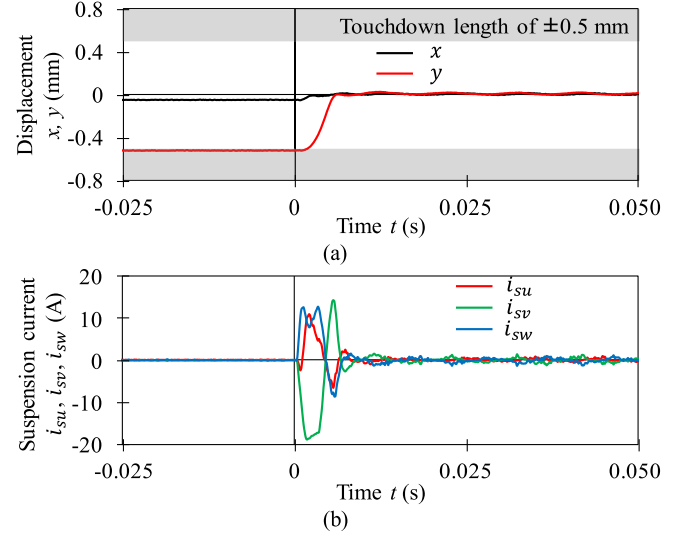


Fig. 17. Experimental result of the magnetic suspension start-up. (a) Radial displacements  $x$  and  $y$ . (b) Three-phase suspension currents.

the suspension currents. The motor speed regulation is also closed-loop-controlled by detecting the rotor rotational position. The reference rotational position  $\theta^*$  is generated from the time integral of the reference rotational speed of the high-speed rotor  $\omega^*$ .

The measured rotor angular position  $\hat{\theta}$  is obtained by the four Hall elements (EQ-733L, Asahi Kasei Microdevices). The rotor angular position is calculated by the arctangent of Hall elements signals in the  $x$ - and  $y$ -axis. Each signal is calculated by the summation of two Hall elements located on opposite sides of the same axis to compensate for the error caused by the rotor radial displacements.

### B. Magnetic Suspension Start-Up

Fig. 17 shows radial rotor displacements and suspension currents  $i_{su}$ ,  $i_{sv}$ , and  $i_{sw}$  during the magnetic suspension start-up. Radial displacement sensor outputs are measured, as well as the suspension currents. The rotor radial position references  $x$  and  $y$  are set to the centered position. At the touchdown condition, the rotor position of  $x$  and  $y$  are  $-0.04$  and  $-0.52$  mm, respectively. These two positions are randomly chosen in the experiment, whereas the rotational angle of the high-speed rotor is set to  $0^\circ$ , where the rotor is aligned to the  $y$ -axis as shown in Fig. 2. At  $t = 0$ , magnetic suspension control is activated, and suspension currents are provided. The limit of suspension currents  $i_{sx}$  and  $i_{sy}$  are set to 14.9 A, that corresponds the current density of  $20.5 \text{ A/mm}^2$ . This current limit is applied for the short time only for the start-up current for 100 ms at the maximum based on the experimental result presented [13]. As a result, the magnetic suspension start-up is successfully achieved with a maximum current of  $i_{sv} = 18.8$  A. In Section IV-C, the start-up current was calculated by FEM as  $i_{sx} = 15.0$  A in  $xy$  coordinates, which is  $i_{sv} = 12.2$  A in  $uvw$  coordinates. Thus, the current measured in this experiment is 53.5% higher than the FEM result because of the transient condition.

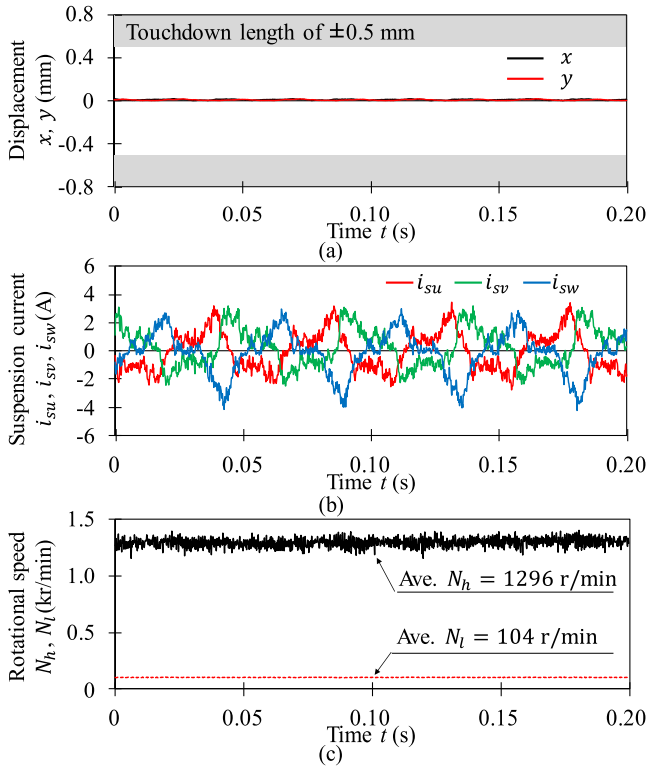


Fig. 18. Experimental results at  $N_h^* = 1300$  r/min while the rotor is magnetically suspended. (a) Radial displacements  $x$  and  $y$ . (b) Three-phase suspension currents. (c) Rotational speed of each rotor.

### C. Magnetic Suspension During Rotation

Fig. 18 shows the waveforms of radial displacements, suspension currents, and rotational speeds of each rotor while the high-speed rotor is magnetically suspended. The radial displacements and suspension currents are measured. The rotational speed of the high-speed rotor is calculated from the derivative of the measured rotor angular position  $\hat{\theta}$ . The rotational speed of the low-speed rotor is detected by a digital tachometer (HT-5500, Ono Sokki). The rotational speeds of both rotors are monitored by an oscilloscope (DLM2024, Yokogawa). In this experiment, the reference speed of the high-speed rotor  $N_h^*$  is 1300 r/min, and the low-speed rotor stably rotates at the synchronized speed of 100 r/min.

As a result, the magnetic suspension and rotation are successfully achieved. The vibrations of suspension currents are small enough compared to the start-up currents. The radial vibration is also small enough compared to touchdown length of  $\pm 0.5$  mm. Therefore, it is experimentally demonstrated that the suspension current is small when the rotor is centered.

In addition, Fig. 18(c) shows that the average speed of the high-speed rotor is 1296 r/min, while the low-speed rotor rotates at 104 r/min. Thus, the high-speed rotor in prototype machine rotates mostly 13 times faster than the low-speed rotor. The difference between theoretical and experimental values is caused by the error introduced by the measurement equipment. Accordingly, the gear ratio  $G_r$  is 13, as designed.

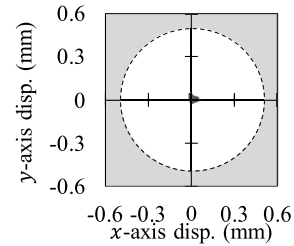


Fig. 19. High-speed rotor displacement (disp.) orbit at  $N_h^* = 7020$  r/min while the rotor is magnetically suspended.

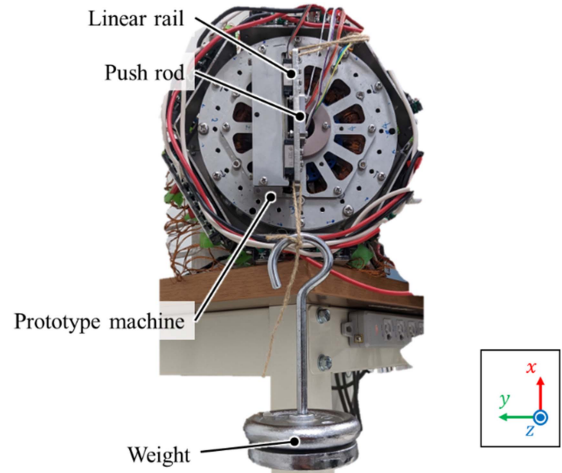


Fig. 20. Experimental setup for measuring radial force  $F_x$ .

Fig. 19 shows the high-speed rotor displacement orbit at  $N_h^* = 7020$  r/min while the rotor is magnetically suspended. The high-speed rotor rotates within the mechanical air gap of 0.5 mm radius. Subsequently, the prototype achieves continuous rotation at  $N_h^* = 7020$  r/min and 540 r/min at the low-speed rotor.

### D. Radial Force Measurement

To compare the analysis and experiment of the prototype machine, a radial force is applied. The suspension current is measured and compared with the FEM analysis.

Fig. 20 shows the experimental setup for radial force measurement. The high-speed rotor is surrounded by the low-speed rotor, which makes it difficult to input force directly from the outside. Thus, the prototype motor was mounted vertically, and an additional device was installed that can apply gravity force as a radial force to the high-speed rotor. This device consists of a push rod mounted on a linear rail that can move in the  $x$ -direction. Hence, the gravity on the high-speed rotor and the push rod is applied in the radial direction of the high-speed rotor. The weight of the push rod assembly is 0.25 kg. Furthermore, the external radial force can be applied by attaching weights. In this experiment, the suspension current is defined as the difference in the zero-suspension current since the radial forces inevitably occur due to mechanical errors, non-uniformity of magnetization, and other factors. The zero-suspension current is defined under the conditions that the prototype is installed horizontally, and the high-speed rotor is suspended at center position. Additionally,

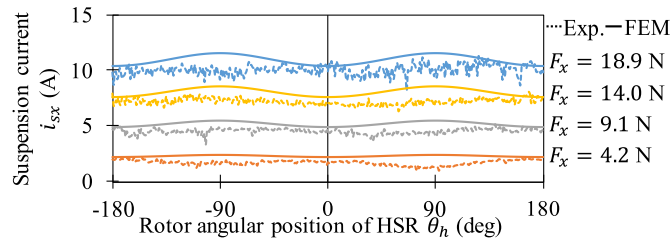


Fig. 21. Experimental results of suspension currents  $i_{sx}$  under different radial forces  $F_x$  with respect to the rotational angular position of the high-speed rotor (HSR)  $\theta_h$ .

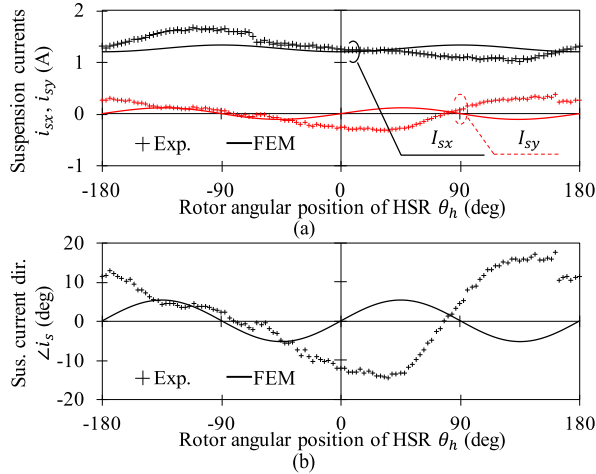


Fig. 22. Experimental results of suspension current and direction under the gravity applied in the  $x$ -axis with respect to the rotational angular position of the high-speed rotor (HSR)  $\theta_h$ . (a) Suspension currents  $i_{sx}$  and  $i_{sy}$  (b) Suspension current direction  $\angle i_s = \tan^{-1}(i_{sx}/i_{sy})$ .

when the weights are applied, the high-speed rotor and the stator are connected through the push rod. Thus, the force in the  $y$ -axis direction  $F_y$  generated by the suspension current  $i_{sx}$  is compensated by the friction force with the push rod.

Fig. 21 shows the suspension current  $i_{sx}$  at a steady state. Suspension currents  $i_{su}$  and  $i_{sv}$  are detected using two current probes and waveforms are captured by the oscilloscope.  $i_{sx}$  and  $i_{sy}$  can be calculated by the measured  $i_{su}$  and  $i_{sv}$  using  $dq$  transformation. The rotor radial position references  $x$  and  $y$  are set to 0 mm. The dotted currents show the experimental result, and the solid currents show the FEM analysis results. As a result, analytical and experimental suspension currents are quite comparable, with only minor differences. The difference was caused by three factors: the hysteresis effect, the reduction of the PM flux in the test machine, and the fluctuation of the magnetic-center-position. According to Figs. 12 and 13, the fluctuation of the suspension characteristics is caused by the flux saturation at the stator back yoke. In the prototype, the flux at the stator back yoke is decreased by the reduction of the PM flux. In the experiment result, the back EMF in the experiment is 10% less. In addition, the fluctuation of the magnetic-center-position has significant influence at small radial force, because the unbalanced magnetic pull force is identical.

Fig. 22 shows the suspension current and its direction under the gravity applied in the  $x$ -axis at a steady state. In Fig. 22(a), the

currents are similar to those of the FEM analysis results. Meanwhile, the result in Fig. 22(b) indicates that the current direction  $\angle i_s = \tan^{-1}(i_{sx}/i_{sy})$  is enlarged compared to the FEM analysis result. This is caused by the mechanical and magnetic errors. In ideal conditions, the magnetic-centered position is constant with respect to the rotational angular position of the high-speed rotor  $\theta_h$ . However, the error of the magnetic-centered position occurred in the experiment. Generally in bearingless motors, the additional weight is applied to increase the suspension current and reduce the influence of the magnetic-centered position error. In contrast, it is quite difficult to add weights directly in this experimental setup. Therefore, the precise measurement of  $\theta_{err}$  requires further investigation.

## VI. CONCLUSION

In this paper, a novel magnetic-gear motor integrated with a high-speed bearingless motor is investigated. The principles of rotation and non-contact magnetic suspension were introduced. The thick stator back yoke was found to have better suspension force and smaller force error angle characteristics. A test machine was built based on FEM analysis and the successful magnetic suspension and rotation were verified.

As a result, the principle of the magnetic-gear motor integrated with a high-speed bearingless motor has been validated for the first time in this work.

## ACKNOWLEDGMENT

The authors are grateful for the academic JMAG software license from JSOL Corporation. The prototype was fabricated by Mr. M. Saito from Motion System Tech.

## REFERENCES

- [1] K. T. Chau, D. Zhang, J. Z. Jiang, C. Liu, and Y. Zhang, "Design of a magnetic-gear outer-rotor permanent-magnet brushless motor for electric vehicles," *IEEE Trans. Magn.*, vol. 43, no. 6, pp. 2504–2506, Jun. 2007.
- [2] L. Chen, A. Thabuis, Y. Fujii, A. Chiba, M. Nagano, and K. Nakamura, "Principle and analysis of radial-force-based swirling actuator for low-speed high-torque applications," *IEEE Trans. Ind. Appl.*, vol. 58, no. 2, pp. 1963–1975, Mar./Apr. 2022.
- [3] K. Atallah, J. Rens, S. Mezani, and D. Howe, "A novel 'pseudo' direct drive brushless permanent magnet machine," *IEEE Trans. Magn.*, vol. 44, no. 11, pp. 4349–4352, Nov. 2008.
- [4] L. L. Wang, J. X. Shen, P. C. K. Luk, W. Z. Fei, C. F. Wang, and H. Hao, "Development of a magnetic-gear permanent magnet brushless motor," *IEEE Trans. Magn.*, vol. 45, no. 10, pp. 4578–4581, Oct. 2009.
- [5] P. O. Rasmussen, T. V. Frandsen, K. K. Jensen, and K. Jessen, "Experimental evaluation of a motor-integrated permanent-magnet gear," *IEEE Trans. Ind. Appl.*, vol. 49, no. 2, pp. 850–859, Mar./Apr. 2013.
- [6] N. Niguchi and K. Hirata, "Torque ripple analysis of a magnetic-gear motor," in *Proc. Int. Conf. Elect. Mach.*, 2012, pp. 787–792.
- [7] E. Marth, G. Jungmayr, W. Amrhein, and F. Jeske, "Magnetic-gear motor in side-by-side arrangement-optimization," in *Proc. IEEE Int. Electric Mach. Drives Conf.*, 2019, pp. 839–846.
- [8] A. Abdel-Khalik, S. Ahmed, and A. Massoud, "A bearingless coaxial magnetic gearbox," *Alexandria Eng. J.*, vol. 53, no. 3, pp. 573–582, 2014.
- [9] F. Zuercher, T. Nussbaumer, W. Gruber, and J. W. Kolar, "Design and development of a 26-pole and 24-slot bearingless motor," *IEEE Trans. Magn.*, vol. 45, no. 10, pp. 4594–4597, Oct. 2009.
- [10] M. Ooshima, "Analyses of rotational torque and suspension force in a permanent magnet synchronous bearingless motor with short-pitch winding," in *Proc. IEEE Power Eng. Soc. Gen. Meeting*, 2007, pp. 1–7.

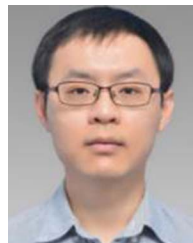


- [11] K. Radman, N. Bulic, and W. Gruber, "Performance evaluation of a bearingless flux-switching slice motor," in *Proc. IEEE Energy Convers. Congr. Expo.*, 2014, pp. 3811–3818.
- [12] N. Watanabe, H. Sugimoto, A. Chiba, T. Fukao, and M. Takemoto, "Basic characteristic of the multi-consequent-pole bearingless motor," in *Proc. Power Convers. Conf.*, 2007, pp. 1565–1570.
- [13] T. Noguchi, H. Sugimoto, Y. Fujii, and A. Chiba, "A novel combined winding and test result of a 20-pole/24-slot consequent-pole bearingless motor with parallel motor winding," *IEEE Trans. Ind. Appl.*, vol. 57, no. 6, pp. 6880–6891, Nov./Dec. 2021.
- [14] W. Gruber, T. Nussbaumer, H. Grabner, and W. Amrhein, "Wide air gap and large-scale bearingless segment motor with six stator elements," *IEEE Trans. Magn.*, vol. 46, no. 6, pp. 2438–2441, Jun. 2010.
- [15] A. Kumashiro, A. Chiba, W. Gruber, W. Amrhein, and G. Jungmayr, "Investigation of a combined electro magnetic structure of bearingless motor and magnetic gear," in *Proc. IEEE Energy Convers. Congr. Expo.*, 2020, pp. 278–284.
- [16] A. Kumashiro, A. Chiba, H. Sugimoto, W. Gruber, W. Amrhein, and G. Jungmayr, "Proposal of magnetic geared motor with bearingless high-speed rotor," in *Proc. 23rd Int. Conf. Elect. Mach. Syst.*, 2020, pp. 1744–1747.
- [17] A. Kumashiro, A. Chiba, W. Gruber, W. Amrhein, and G. Jungmayr, "Novel reluctance-type magnetic geared motor with integrated with high-speed bearingless motor," in *Proc. Int. Power Electron. Conf.*, 2022, pp. 1762–1768.
- [18] A. Kumashiro, A. Chiba, W. Gruber, W. Amrhein, and G. Jungmayr, "Optimization of stack length in magnetic-geared motor with magnetically suspended high-speed rotor," in *Proc. IEEE Energy Convers. Congr. Expo.*, 2022, pp. 1–7.
- [19] S. Hasanpour, M. C. Gardner, M. Johnson, and H. A. Toliyat, "Comparison of reluctance and surface permanent magnet coaxial magnetic gears," in *Proc. IEEE Energy Convers. Congr. Expo.*, 2020, pp. 307–314.
- [20] W. N. Fu and S. L. Ho, "A quantitative comparative analysis of a novel flux-modulated permanent-magnet motor for low-speed drive," *IEEE Trans. Magn.*, vol. 46, no. 1, pp. 127–134, Jan. 2010.
- [21] R. Qu, D. Li, and J. Wang, "Relationship between magnetic gears and vernier machines," in *Proc. IEEE Int. Conf. Elect. Mach. Syst.*, 2011, pp. 1–6.
- [22] L. Xu, W. Zhao, G. Liu, and C. Song, "Design optimization of a spoke-type permanent-magnet vernier machine for torque density and power factor improvement," *IEEE Trans. Veh. Technol.*, vol. 68, no. 4, pp. 3446–3456, Apr. 2019.
- [23] J. Chen, J. Zhu, and E. L. Severson, "Review of bearingless motor technology for significant power applications," *IEEE Trans. Ind. Appl.*, vol. 56, no. 2, pp. 1377–1388, Mar./Apr. 2020.
- [24] J. Asama, T. Fukao, A. Chiba, A. Rahman, and T. Oiwa, "A design consideration of a novel bearingless disk motor for artificial hearts," in *Proc. IEEE Energy Convers. Congr. Expo.*, 2009, pp. 1693–1699.
- [25] K. Aiso, K. Akatsu, and Y. Aoyama, "A novel reluctance magnetic gear for high-speed motor," *IEEE Trans. Ind. Appl.*, vol. 55, no. 3, pp. 2690–2699, May/Jun. 2019.
- [26] J. Asama, T. Asami, T. Imakawa, A. Chiba, A. Nakajima, and M. A. Rahman, "Effects of permanent-magnet passive magnetic bearing on a two-axis actively regulated low-speed bearingless motor," *IEEE Trans. Energy Convers.*, vol. 26, no. 1, pp. 46–54, Mar. 2011.
- [27] J. Asama, D. Kanehara, T. Oiwa, and A. Chiba, "Development of a compact centrifugal pump with a two-axis actively positioned consequent-pole bearingless motor," *IEEE Trans. Ind. Appl.*, vol. 50, no. 1, pp. 288–295, Jan./Feb. 2014.
- [28] S. Silber, W. Amrhein, P. Boesch, R. Schoeb, and N. Barletta, "Design aspects of bearingless slice motors," *IEEE Trans. Mechatronics*, vol. 10, no. 6, pp. 611–617, Dec. 2005.
- [29] T. Reichert, T. Nussbaumer, and J. W. Kolar, "Bearingless 300-W PMSM for bioreactor mixing," *IEEE Trans. Ind. Electron.*, vol. 59, no. 3, pp. 1376–1388, Mar. 2012.
- [30] Q. Li, P. Boesch, M. Haefliger, J. W. Kolar, and D. Xu, "Basic characteristics of a 4 kW permanent-magnet type bearingless slice motor for centrifugal pump system," in *Proc. IEEE Int. Conf. Elect. Mach. Syst.*, 2008, pp. 3037–3042.
- [31] G. Jungmayr, J. Loeffler, B. Winter, F. Jeske, and W. Amrhein, "Magnetic gear: Radial force cogging torque skewing and optimization," *IEEE Trans. Ind. Appl.*, vol. 52, no. 5, pp. 3822–3830, Sep./Oct. 2016.
- [32] D. Steinert, T. Nussbaumer, and J. W. Kolar, "Evaluation of one- and two-pole-pair slotless bearingless motors with toroidal windings," *IEEE Trans. Ind. Appl.*, vol. 52, no. 1, pp. 172–180, Jan./Feb. 2016.
- [33] E. Gobl, W. Amrhein, and H. Mitterhofer, "Slotless bearingless high speed disk drive designed for speeds beyond 100krpm," in *Proc. IEEE 12th Int. Conf. Power Electron. Drive Syst.*, 2017, pp. 1,017–1,023.
- [34] J. Asama, R. Nakamura, H. Sugimoto, and A. Chiba, "Evaluation of magnetic suspension performance in a multi-consequent-pole bearingless motor," *IEEE Trans. Magn.*, vol. 47, no. 10, pp. 4262–4265, Oct. 2011.



**Akira Kumashiro** (Graduate Student Member, IEEE) was born in Oita, Japan, in 1996. He received the B.S. degree in electrical engineering from the Electrical, Electronics Information Engineering Major, National Institute of Technology, Oita College, Oita, Japan, in 2019, and the M.S. degree in electrical engineering in 2021 from the Tokyo Institute of Technology, Tokyo, Japan, where he is currently working toward the Ph.D. degree. He is involved in bearingless magnetic-geared motor project with Tokyo Institute of Technology. His research interests

include bearingless motor and magnetic-geared motor.



**Lingyu Chen** (Member, IEEE) received the B.E. degree in electrical engineering from Sichuan University, Chengdu, China, in 2014, and the M.S. degree in power electronics and drives from the South China University of Technology, Guangzhou, China, in 2017. He is currently working toward the Ph.D. degree with the Chiba Lab, Department of Electrical and Electronic Engineering, Tokyo Institute of Technology, Tokyo, Japan. His research interests include the design and analysis of low-speed high-torque actuators.



**Yusuke Fujii** (Member, IEEE) received the B.S., M.S., and Ph.D. degrees in mechanical engineering from Shizuoka University, Hamamatsu, Japan, in 2015, 2017, and 2020, respectively.

In 2019, he was a Visiting Scholar with the University of Wisconsin-Madison, Madison, WI, USA, for half a year, where he was involved in bearingless induction motors. He is currently an Assistant Professor with the Department of Electrical and Electronic Engineering, Tokyo Institute of Technology, Tokyo, Japan. His research interests include bearingless motors, magnetic bearings, and motor drives.

Dr. Fujii is a Member of The Institute of Electrical Engineers of Japan and the Japan Society of Mechanical Engineers.



**Akira Chiba** (Fellow, IEEE) received the B.S., M.S., and Ph.D. degrees in electrical engineering from the Tokyo Institute of Technology, Tokyo, Japan, in 1983, 1985, and 1988, respectively. He is studying magnetically suspended bearingless AC motors, super high-speed motor drives, and rare-earth-free-motors for hybrid and pure electric vehicles. In 1988, he joined the Department of Electrical Engineering, Faculty of Science and Technology, Tokyo University of Science, Tokyo, Japan. Since 2010, he has been a Professor with the School of Engineering, Tokyo

Institute of Technology, Tokyo. He was the Department Head of Electrical and Electronics Department between 2014 and 2016 and led MOOC project of the introduction of Electrical and Electronics Engineering, released in May 2017 through EDX. He has led active learning with Internet Handbook application in undergraduate and graduate course lectures. He is currently the Head of the Electrical and Electronics course in the graduate school. He has authored or coauthored more than 1229 papers, including the first book on *Magnetic Bearings and Bearingless Drives* from Elsevier in 2005. Dr. Chiba was the recipient of the First Prize Paper Award from the Electrical Machine Committee in the IEEE IAS in 2011 on a rare-earth-free motor, second and third place Best Paper Awards in IEEE Transactions on Energy Conversion in 2016 and 2017, respectively, IEEJ Prize Paper Awards in 1998, 2005, 2018, 2023, and 2020 IEEE Nikola Tesla Award, that is one of the IEEE Technical Field Awards. In 2023, he was also the recipient of the IEEE PES Cyril Veinott Electromechanical Energy Conversion Award and 2020 Distinguished Service Award from the Electric Machinery Committee in IEEE PES. He was the Secretary, Vice-Chair, Vice-Chair-Chair-Elect, Chair, and Past Chair in the Motor Sub-Committee in the IEEE PES during 2007/2016. He has organized the Panel sessions and the combo sessions to activate the motor sub-committee. He was the Technical Co-Chair in IEEE IEMDC 2017 held in Miami, FL, USA, that was hosted by IEEE PES. He was the Editor of IEEE TRANSACTIONS ON ENERGY CONVERSION during 2013/2023. He was the Secretary, Vice Chair, Chair, and Past Chair in IEEE-IAS Electric Machine Committee during 2016/2023. He improved the relationship between PES and IAS electric machine related committees. He was the ECCE Vice-Chair during 2016/2019. He was a TCPRC and an Associate Editor for the IEEE TRANSACTIONS ON INDUSTRY APPLICATIONS during 2020/2021 and 2011/2019, respectively. He was one of the IEEE IAS Fellow Committee Executives from 2017 to 2020. He was the Chair in IEEE-IAS Japan Chapter during 2010/2011. He was a Member, the Chair, and Past-Chair in the IEEE Nikola Tesla Technical Field Award Committee during 2009/2014. He was a Member in IEEE Power Medal Award Committee during 2021/2023. He was the Founding Chair in the Motor Technical Committee in Japan Society of Automotive Society during 2012/2018. He was the Chair of the IEE-Japan Electric Machine Committee from 2020 to 2023. He has been an Examiner in the Nagamori Award since 2015.



**Wolfgang Amrhein** was born in Aschaffenburg, Germany, in 1957. He received the M.Sc. (Dipl.-Ing.) degree in electrical engineering from the Technical University Darmstadt, Darmstadt, Germany, in 1982, and the Ph.D. (Dr. sc.techn.) degree from the Swiss Federal Institute of Technology Zurich, Zurich, Switzerland, in 1988. From 1982 to 1990, he was a Scientific Assistant with the Swiss Federal Institute of Technology Zurich. In 1990, he joined Papst Motoren GmbH, St. Georgen, Germany, where he became the Head of the Development Department in 1992. Since

1994, he has been a Professor and subsequently the Head of the Institute of Electrical Drives and Power Electronics, Johannes Kepler University (JKU), Linz, Austria. From 2000 to 2007, he was a Scientific Head of the Linz Center of Competence in Mechatronics, Austria, together with Prof. R. Scheidl. Since 2010, he has been the Head of the JKU HOERBIGER Research Institute for Smart Actuators, JKU. His research interests include electric drives, with special emphasis on small electric motors, magnetic bearing systems, bearingless motors, and power electronics.



**Gerald Jungmayr** was born in Wels, Austria, in 1977. He received the M.Sc. (Dipl.-Ing.) degree in mechatronics and the Ph.D. degree from the Johannes Kepler University (JKU), Linz, Austria, in 2003 and 2008, respectively. From 2004 to 2017, he was a Researcher with the Institute of Electrical Drives and Power Electronics, JKU, and became the Deputy Chair in 2014. Since 2017, he has been a Senior Researcher with the Linz Center of Mechatronics. His main research interests include passive and active magnetic bearings, magnetic gears, and electric drives.



**Wolfgang Gruber** (Senior Member, IEEE) received the Dipl.-Ing. (M.Sc.) degree in mechatronics and Dr. techn. (Ph.D.) degree in technical sciences from Johannes Kepler University (JKU), Linz, Austria, in 2004 and 2009, respectively. Since 2012, he has been an Assistant Professor, since 2018, an Associate Professor, and since 2021, a Full Professor with the Institute of Electrical Drives and Power Electronics, JKU. Since 2004, he has also been a Senior Researcher with the R&D Company Linz Center of Mechatronics GmbH (LCM), Linz, Austria. He has developed the

bearingless segment motor, reluctance motor, flux switching motor, and PM Vernier motor. His research interests include new topologies for bearingless slice motors, their design, setup, and control. Prof. Gruber was the recipient of the international Nagamori Award in 2015.